Iraqi National Journal of Earth Science

www.earth.uomosul.edu.iq

Lithological Discrimination and Lineaments Extraction Using Landsat-8 and Sentinel-2A Data, A Case Study of Gabal Abu Hamr and Gabal Abu Kharif Area, North Eastern Desert, Egypt

Mohammed A. Soliman [1*] (iD), **Mohamed A. Yehia** [2], **Ali A. Omran** [3], **Hassan I. El Sundoly** [4],

Mahmoud M. Salem [5] (iD) , **Karim W. Abdelmalik** [6] (iD)

[1,3,4,5] *Nuclear Materials Authority of Egypt, P.O. Box 530, El Maadi, Cairo, Egypt.*
[2,6] *Department of Geology, College of Science, University of Ain Shams, Cairo, Egypt.*

Article information	ABSTRACT
  Correspondence: **Name:** Mohammed A. Soliman Email: mabdelrahman199_p@sci.asu.edu.eg	The current work emphasizes the ability of Landsat-8 (L8) and Sentinel-2A (S2A) satellite data through image processing to discriminate lithology and extract lineaments in the area of Gabal Abu Hamr and Gabal Abu Kharif, Northeastern Desert, Egypt. Different image processing methodologies are utilized to both Landsat-8 and Sentinel-2A images such as False-Color Composites (FCC), analysis as Minimum Noise Fraction (MNF), Principal (PCA), where largest variation recorded is in the first three PC bands (more than 99%), and Independent Component (ICA) and mathematical means as Band Algebra. Furthermore, image classification techniques, including Maximum Likelihood (MLC) and Support Vector Machine (SVM), are utilized for identifying pixels with similar characteristics, which support the process of separating rock units in the current study. These techniques can discriminate the rocks of the study area, especially the older granitoid rocks, which are difficult to separate in the field due to the mineral affinity between them. The manual and automatic lineaments extraction methods by visual interpretation and Directional Filtering via the LINE algorithm in PCI Geomatica shed light on the common lineaments' directions within the study area, exhibiting trends in the NE-SW and E-W, followed by a trend in the N-S direction.

التمييز الصخري واشتقاق التراكيب الخطية باستخدام بيانات القمر لاندسات-8 والقمر سنتينل-A2، دراسة حالة لمنطقة جبل أبو همر وجبل أبو خريف، شمال الصحراء الشرقية، مصر

محمد سليمان [1]* ، محمد يحيى [2] ، علي عمران [3] ، حسن الصندولي [4] ، محمود سالم [5] ، كريم عبدالملك [6]

[1,3,4,5] *هيئة المواد النووية، القاهرة، مصر .*

[2,6] *قسم الجيولوجيا، كلية العلوم، جامعة عين شمس، القاهرة، مصر .*

الملخص	معلومات الارشفة

يهدف العمل الحالي إلى بيان قدرة القمر الصناعي (لاندسات-8) والقمر (سنتينل-2أ) في التمييز الصخري واشتقاق التراكيب الخطية لمنطقة جبل أبو همر وجبل أبو خريف، شمال الصحراء الشرقية، مصر. ولقد تم إجراء العديد من عمليات المعالجة لمرئيات الأقمار الصناعية سالفة الذكر سواء كانت معالجة بصرية ممثلة في FCC أو طرق معالجة تحليلية مثل PCA, ICA, MNF والتي أثبتت فاعليتها، حيث أن معدل تحميل البيانات قد يتخطى نسبة 99% للثلاث نطاقات الأولى، الأمر الذي يساعد في اختيار تلك النطاقات ومعالجتها في الحصول على أفضل تمييز صخري لصخور منطقة الدراسة. كما تمت معالجة إحصائية باستخدام معادلات حسابية مثل BR، بالإضافة إلى طريقة المعالجة باستخدام تقنية تصنيف الصورة عن طريق SVM و MLC والتي من خلالها تم الحصول على التمييز الصخري لمنطقة الدراسة. من جهةٍ أخرى، تم استخدام مرئيات الأقمار الصناعية في اشتقاق التراكيب الخطية بطريقة يدوية وأوتوماتيكية للحصول على الاتجاهات السائدة في منطقة الدراسة والتي تتمثل في اتجاه شمال شرق-جنوب غرب متبوعاً باتجاه شرق-غرب.

Introduction

Natural resources exploration over large areas through traditional exploration techniques includes significant financial risks as well as time- and effort-consuming, and may not be economically feasible; so, resorting to remote sensing techniques, including satellites and airborne data, may offer efficient and cost-effective tools for geological mapping and mineral exploration. Consequently, they can contribute to the effectiveness of earth resources exploration programs, leading to well-founded results and conclusions. With the first appearance of multispectral satellites, such as Landsat-8 and Sentinel-2A, many studies related to geology and mineralogy were conducted that analyze the absorption properties of minerals, providing a scientific foundation for the interpretation of spectral data acquired through remote sensing (Gaffey, 1985; Crowley, 1986). The chosen Landsat-8 and Sntinel-2A data in this study is due to their availability, wide spectral coverage (11 bands in L8 and 12 in S2A) and their relatively good spatial resolution (15 m in L8 and 10 m in S2A); consequently, they will be suitable in the mapping of the geological rock unites and alteration zones.

The present work aims to highlight the pivotal role, remotely sensed data, exemplified by Landsat-8 and Sentinel-2A images that greatly helps in discerning the lithological characteristics of igneous rocks within an arid environment; also, this study aims to evaluate

their effectiveness in rock mapping and assess their capability to distinguish between rocks with similar mineral compositions. This discrimination is accomplished through the strategic application of FCC, MNF, PCA, ICA, Band Algebra, and image classification methods. Moreover, the practicability of manual and automatic extraction of lineaments using the interpretation of the images through visual analysis and the LINE algorithm will be tested to determine the efficiency of multispectral data in automatically identifying linear structures and to compare its accuracy with manual identification methods.

This study will cover the area of G. Abu Hamr and G. Abu Kharif area, North Eastern Desert, Egypt. This area is situated approximately 60 km west of Safaga City, along the coastline of the Red Sea, where it covers about 185 km^2 and is bounded by latitudes $26°46'$ - $26°55'$ N and longitudes $33°23'$ - $33°31'$ E (Fig. 1).

Several detailed geological studies have been conducted in this area, such as Mohamed et al. (2003), who identified the granites of G. Abu Hamr as syenogranites and alkali-feldspar granites. They observed that the granitic mass of G. Abu Hamr is elongated in a NE-SW direction, likely due to its intrusion being structurally controlled by pre-existing fractures trending NE-SW (Qena-Safaga shear zone, as mentioned by El Gaby in 1994). El Sundoly (2016) further analyzed fault slip data from G. Abu Hamr and suggested that most faults are compressional strike-slip fault systems, with a minority being extensional (normal) faults, thus indicating a significant structural influence on the granite formation. Also, the G. Abu Kharif area was investigated by Abdel Wanees et al. (2021), who reported that G. Abu Kharif comprises three distinct granitic magma suites: Cryogenian granodiorite suite, Ediacaran monzogranite suite, and Cambrian alkali riebeckite granite suite. However, none of these studies had utilized the remote sensing technique. Therefore, it is likely that for the first time, the remote sensing technique is employed to discriminate the lithology of the G. Abu Hamr and G. Abu Kharif area. It is worth noting that this technique is used to separate the rocks of some areas adjacent to the study area, such as the Gabal Ras Abda area (Salem et al., 2024), and other distant areas (Abdelmalik et al., 2023).
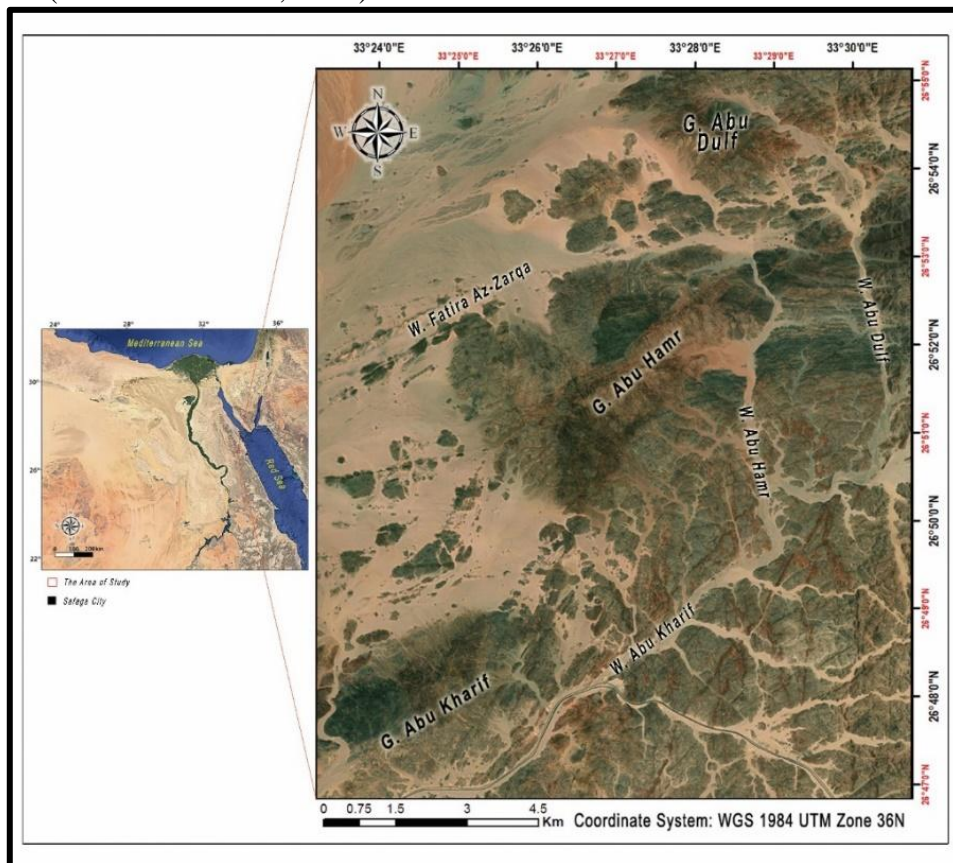

Fig. 1. Location map of G. Abu Hamr and G. Abu Kharif area, North Eastern Desert, Egypt.

Materials and Methods

1- Image Pre-Processing and Processing

The step of image pre-processing prepares data for subsequent analysis of processing steps, where the pre-processing procedures have been carried out to mitigate sensor and atmospheric effects to the greatest extent possible and align the imagery with a precise topographic base. The image processing is crafted to convert the multispectral image data format into an image that either enhances the contrast between noteworthy targets and the background or provides information about the composition of specific pixels in the image. So, the possible forms of digital image pre-processing and processing are classified into the following procedures:

i. *FLAASH - Atmospheric Correction*

The data are additionally calibrated to spectral radiance, subsetted, and transformed from digital number to reflectance employing the FLAASH atmospheric correction model. FLAASH technique is used only on Landsat-8 in current work because the cloud-free image from Sentinel-2A is automatically subjected to atmospheric correction and orthorectification through SNAP software package, where bands (1, 9, and 10) are specifically configured to visualize atmospheric effects (Drusch, et al., 2012); so, the lithological classification in this study excludes the use of bands (1, 9, and 10).

ii. *Minimum Noise Fraction* (MNF)

This technique is used in the pre-processing or noise reduction step to ascertain the intrinsic dimensions of image data, segregate and equalize noise within the data, and then to diminish the computational demands for post-processing (Green et al., 1988). The MNF components with eigenvalues less than one are excluded from the data as noise to improve the subsequent spectral processing (Jensen, 1986). The resulting eigenimages, which exhibit reduced noise, can then be chosen to create an RGB composite image. This composite image is utilized for detecting alteration minerals and general lithological discrimination (Pour and Hashim, 2012).

iii. *Principal Component Analysis* (PCA)

PCA is a comprehensive analytical technique employed for correlated multivariable datasets. It involves transforming the original data organized along the axes of greatest variability to display maximum contrast from multiple spectral bands using only three primary display colors (Vincent, 1997). The number of the resulting PC-bands correspond to the number of input spectral bands. Typically, the first three high-order PCs (1, 2, and 3) capture more than 99% of the spectral information, while the lower-order ones tend to have lower ratios (Al Amri et al., 2010).

iv. *Independent Component Analysis* (ICA)

ICA, in its formulation, bears similarities to PCA, but conversely, its objective is to identify a set of independent components rather than orthogonal ones. It relies on high-level statistics and possesses the capability to differentiate between objects of interest even when they occupy only a small portion of the image pixels (Kumar et al., 2015).

v. *Band Ratio and Band Algebra*

A crucial enhancement technique employed for minerals mapping is band ratio (BR), wherein a mathematical formula is devised and applied to validate the investigated target while mitigating shadow effects induced by topography (Crowley et al., 1989). BR images augment material contrast by dividing the brightness values at peaks and troughs in a reflectance curve. Many authors have utilized the correlation between measured spectral signature curves and remotely sensed images to identify and map various rock types. (e.g., Abdelmalik and Abd-Allah, 2018; Farag et al., 2019; Fowler et al., 2020; Abdelmalik, 2020; El-Hadidy et al., 2022; Ghoneim et al., 2022; Bety, 2022; Jemy et al., 2023). Spectral signature curves obtained by

ASD TerraSpec Halo Mineral Identifier are carefully studied to determine their behavior as well as the sensitive bands for their samples, and used for illustrating and creating the best mathematical formula to enhance and map the lithological map.

2- Image Classification

Image classification is one of the most common and advanced analyses of multispectral remote sensing data to output thematic maps that offer a depiction of the spatial distribution within a given area (Foody and Mathur, 2004). Lithological classification is conducted using the two-machine learning methods as follows:

i. *Maximum Likelihood Classification* (MLC)

MLC is widely recognized as a frequently used supervised classifier in remote sensing techniques (Zhang et al., 2007) and has been acknowledged as an effective technique for lithological mapping (Gomez et al., 2005). This technique operates under the assumption that the probability density function for each class is multivariate (Ge et al., 2018) and assigns an unknown pixel to the class that holds the highest probability of belonging (Chen et al., 2007).

ii. *Support Vector Machine* (SVM)

SVM is also used as a supervised machine learning algorithm, which is based on statistical learning theory (Mondal et al., 2012). It is originally designed as a binary classifier; SVM strives to separate two classes by establishing boundaries between them. The process can be reiterated to distinguish several undefined classes (Maxwell et al., 2018).

3- Lineaments Extraction

Surface lineaments could be defined as a mappable, linear feature or a combination of linear features on the surface. These features exhibit a straight or slightly curved alignment, distinct from the adjacent pattern of features, and likely reflect both surface and subsurface phenomena (O'Leary et al., 1976). Gupta (2003) condensed the definition of lineaments in various geological features encompassing shear zones, faults, joints, fold axial traces, rift valleys, fracture traces, and alignments associated with topographic, vegetation, or soil tonal changes. The adoption of remote sensing techniques with radar data has proven highly efficient in determining many structural discontinuities, especially the derivation of linearity and determining their density or direction (Bety et al., 2022).

The lineament study aims to identify the most effective approach for lineament analysis through manual and automatic methods. For automatic lineament extraction, the data utilized include the spectral panchromatic band 8 of Landsat-8 and band 2 of Sentinel-2A. These bands have been chosen in the process of lineament extraction analysis present in the study area as a result of their high spatial resolution represented by 15 m of L8 and 10 m of S2A.

Results

1- Lithological Discrimination

For L8 and before processing methods, the FLAASH technique needs to use an equation to resample all data at a range from 0 to 1 surface reflectance (ENVI Tutorials, 2000) (Table 1).

$$(B1\ le\ 0)*0+(B1\ ge\ 10000)*1+(B1\ ge\ 0\ and\ B1\ lt\ 10000)*float(B1)/10000$$

where; (*B1 le 0*)*0 $\longrightarrow$ if the pixel value ≤ 0 , multiply it by 0;

(*B1 ge 10000*)*1 $\longrightarrow$ if pixel value ≥ 10000, multiply it by 1;

(*B1 gt 0 and B1 lt 10000*) * *float (B1) / 10000* $\longrightarrow$ if pixel value $> 0 < 10000$, multiply it by its float value and divide the result by 10000.

The resulting enhancement of the FLAASH image is combined as FCC-742 RGB bands to provide effective lithological discrimination in arid regions (Sabins, 1987) (Fig. 2).

Mohammed A. Soliman *et al*…….

Table 1: Statistical data of FLAASH-atmospheric correction of Landsat-8 bands before and after applying of resampling equation.

Basic Stats		Min	Max	Mean	Std. Dev
Before	B 1	-398	3975	889.622513	534.755363
	B 2	-439	4080	935.475434	587.686407
	B 3	-396	5534	1454.117741	873.289877
	B 4	-382	7055	2007.876217	1173.736367
	B 5	-226	7711	2318.104395	1314.642933
	B 6	-21	8347	2699.328428	1508.527820
	B 7	0	8036	2517.286308	1408.728217
After	B 1	0.000000	0.397500	0.089061	0.053301
	B 2	0.000000	0.408000	0.093790	0.058352
	B 3	0.000000	0.553400	0.145545	0.087097
	B 4	0.000000	0.705500	0.200829	0.117301
	B 5	0.000000	0.771100	0.231813	0.131460
	B 6	0.000000	0.834700	0.269933	0.150853
	B 7	0.000000	0.803600	0.251729	0.140873

i. *The Minimum Noise Fraction* (MNF)

MNF technique is applied to Landsat-8 bands to detect lithological units of the area, where the focus is on eigenvalues greater than one, and an RGB color composite image is then created by assigning high-value MNF eigenimages. As shown in Table 2, the statistical analysis of MNF-transformed bands of Landsat-8 reveals that MNF eigenimages of bands 5, 6, and 7 are unsuitable for assigning an RGB color composite. This conclusion is drawn from their percentage of eigenvalues being close to 1. As the component number increases, the MNF component images display a consistent decline in image quality (Chen et al., 2007). So, the remaining eigenimages consist of MNF bands (1, 2, and 3) of Landsat-8 used for assigning the RGB color composite image (Fig. 3).

Table 2: The eigenvalue percentages for all MNF bands derived from Landsat-8 bands.

	Stats	Min	Max	Mean	Std. Dev	Eigenvalues	%
MNF-L8	B 1	0.000000	0.607700	0.061338	0.056241	24.126242	40.6
	B 2	0.000000	0.623800	0.060557	0.061945	13.020015	21.9
	B 3	0.000000	0.756600	0.089782	0.097945	8.565169	14.4
	B 4	0.000000	0.916500	0.119748	0.131040	6.517605	10.9
	B 5	0.000000	1.000000	0.139464	0.152139	3.388726	5.7
	B 6	0.000000	1.000000	0.178896	0.191879	2.750056	4.6
	B 7	0.000000	0.928700	0.160691	0.169733	1.115693	1.9

ii. *Principal Component Analysis* (PCA)

PCA is applied separately on two datasets, where PCs are calculated using Landsat-8 and Sentinel-2A input spectral bands (Tables 3 and 4). The applied PCs are intended to extract the lithology of the area. Statistics of PCs on L8 and S2A are computed, and hence, the percentages of data variation are produced. The largest variation recorded is in the first PC image (97.48 % of L8) and (97.7 % of S2A). The resulting PC images are generated and enhanced to apply a simple transform (Fig. 4).

Table 3: The resulting PCA-variance extracted from the analysis of Landsat-8 bands.

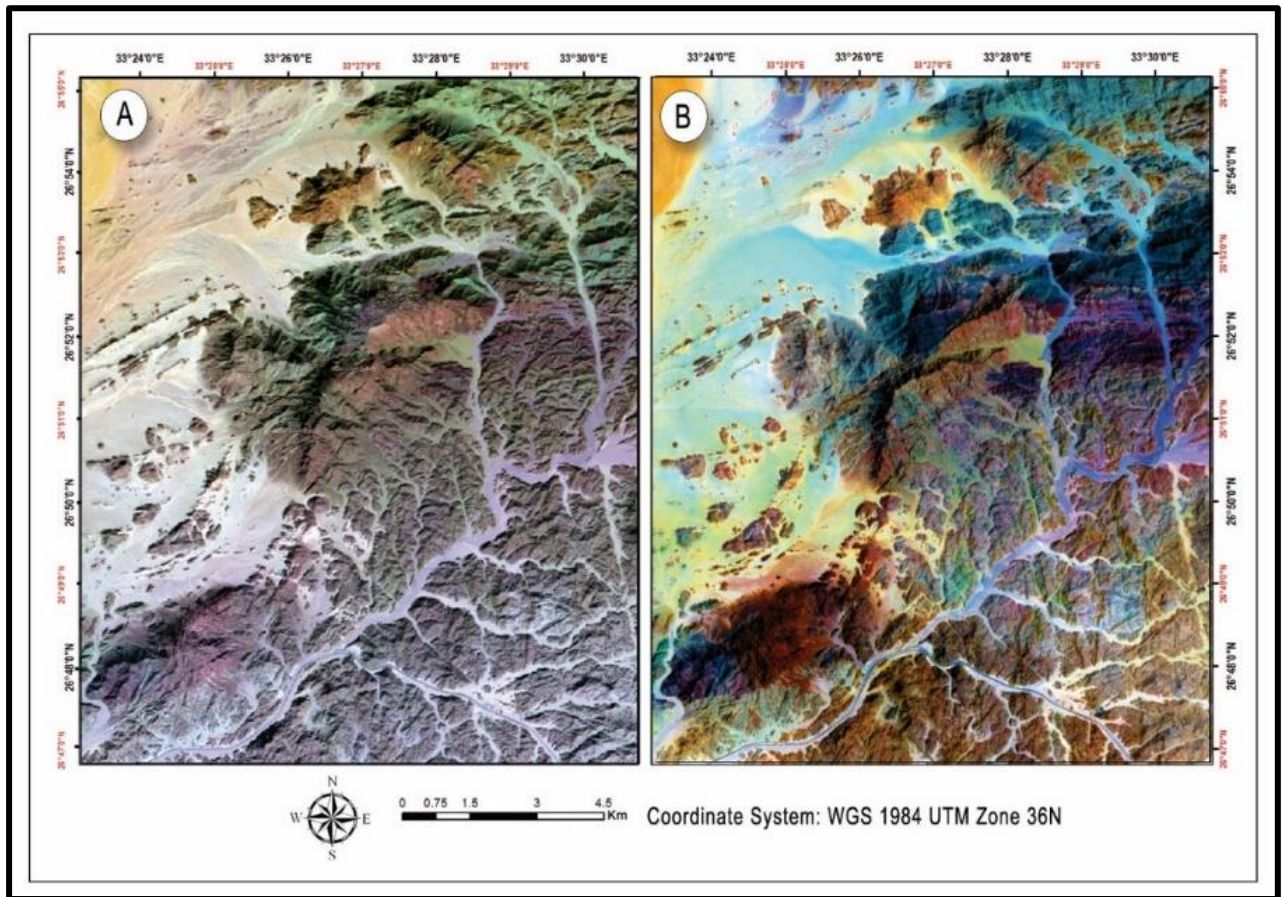|	Stats	B1	B2	B3	B4	B5	B6	B7	Variance %
PCA-L8	PC1	0.998	-0.046	-0.006	0.009	0.005	0.002	0.002	97.48
	PC2	0.046	0.998	-0.002	0.028	0.007	0.009	0.003	2.11
	PC3	0.007	0.004	0.995	-0.064	-0.034	0.049	-0.034	0.274
	PC4	0.011	0.025	-0.080	-0.839	-0.513	0.152	-0.011	0.073
	PC5	-0.001	0.007	0.002	-0.509	0.831	0.013	0.220	0.041
	PC6	0.005	0.014	0.030	-0.156	-0.032	-0.969	-0.183	0.017
	PC7	0.001	0.002	-0.040	-0.074	0.204	0.185	-0.957	0.005

Fig. 2. A) Before, and B) after applying of enhancement technique (saturation stretching) in FCC 742 in RGB image and raising its spatial resolution using high-resolution panchromatic band 8 of Landsat-8 imagery.

Table 4: The resulting PCA-variance extracted from the analysis of Sentinel-2A bands.

	Stats	B2	B3	B4	B5	B6	B7	B8	B8a	B11	B12	%
PCA-S2A	PC1	-0.54	0.15	-0.2	0.8	0.01	0.001	0.01	0.002	0.001	-0.002	97.7
	PC2	0.13	-0.07	0.06	0.1	0.98	0.06	-0.05	0.02	-0.003	-0.007	1.48
	PC3	0.62	-0.13	0.2	0.5	-0.19	0.22	-0.47	-0.07	-0.01	0.023	0.44
	PC4	-0.05	-0.12	-0.02	-0.02	-0.03	0.92	0.37	0.001	0.02	-0.02	0.20
	PC5	-0.25	-0.07	-0.11	-0.18	0.001	0.18	-0.56	0.72	0.16	-0.07	0.05
	PC6	0.11	0.16	0.57	0.18	-0.04	-0.11	0.41	0.59	-0.28	0.026	0.04
	PC7	0.32	-0.36	-0.69	0.12	-0.02	-0.14	0.26	0.32	-0.28	0.068	0.03
	PC8	0.06	-0.2	0.06	0.09	-0.01	-0.1	0.21	0.12	0.74	0.578	0.02
	PC9	-0.26	-0.84	0.31	0.06	-0.05	-0.14	0.03	-0.08	-0.01	-0.314	0.02
	PC10	0.24	0.18	-0.11	0.09	-0.01	-0.08	0.22	0.1	0.52	-0.745	0.02

iii. Independent Component Analysis (ICA)

Applying the ICA technique in Sentinel-2A data (Landsat-8 has no characteristic spectral features in the current study using this technique) produces new "bands" called independent components (ICs) with each component emphasizing one or multiple lithologies. Furthermore, these ICs can be visualized as an FCC image by assigning them to an RGB display (Fig. 5).
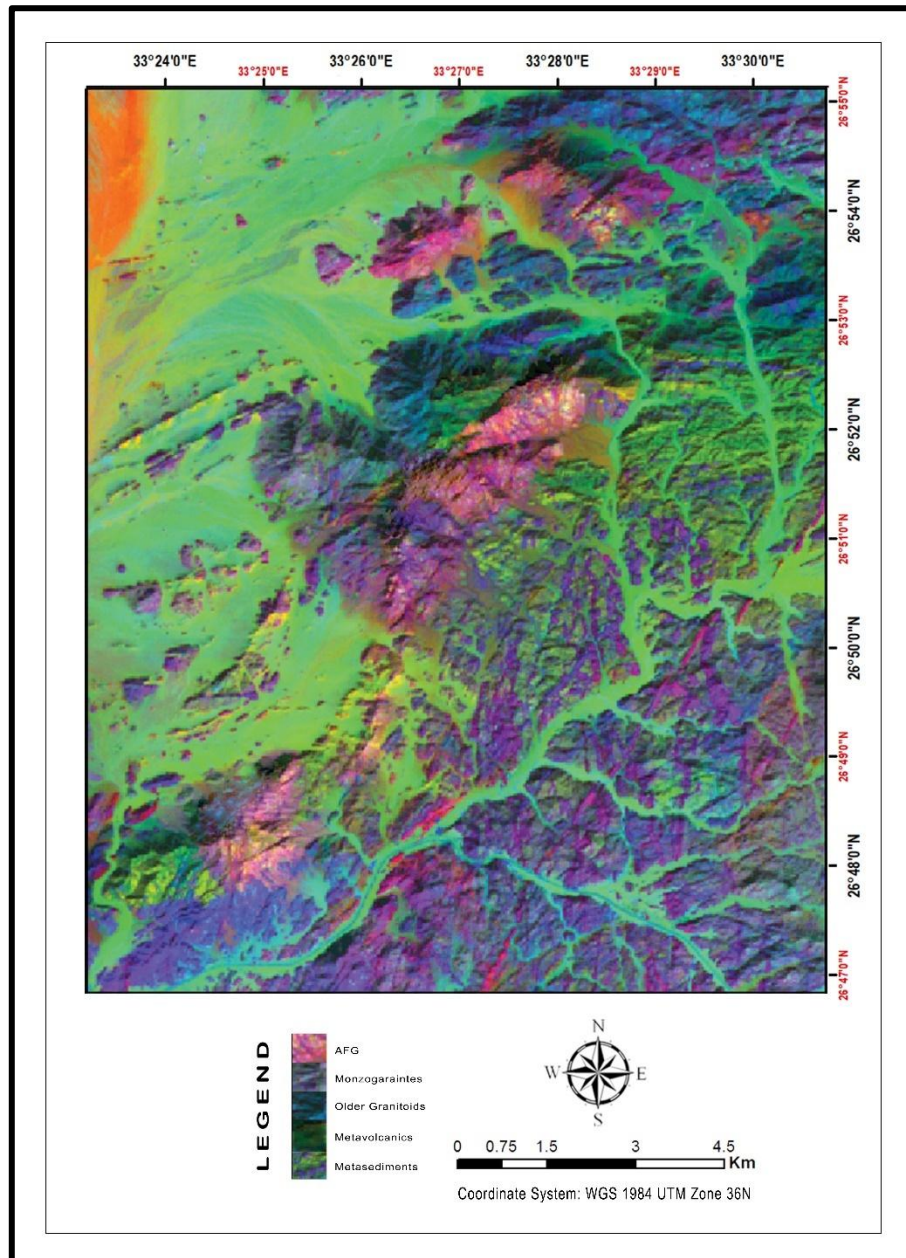
Fig. 3. Lithological discrimination via Landsat-8 data MNF1, MNF2, and MNF3 in RGB, respectively.

iv. Band Ratio and Band Algebra

The measured reflectance profile of the spectral signature of each rock type underwent a resampling algorithm to align with the spectral characteristics and specifications of Landsat-8 and Sentinel-2A sensors, and is illustrated in Figure 6. Several band ratios and algebra have been used to clarify the lithology of the investigated area, and after many attempts of tries and errors, some equations have been reached, through which a separation of the rock types is made. Utilizing the chosen sensitive and highly responsive bands derived from the analyzed spectral behavior along with the resampled spectral curve, three band ratios for Landsat-8 and five band ratios for Sentinel-2A are formulated. These ratios are developed to provide clear illustrations and facilitate the mapping of lithology in the studied area.
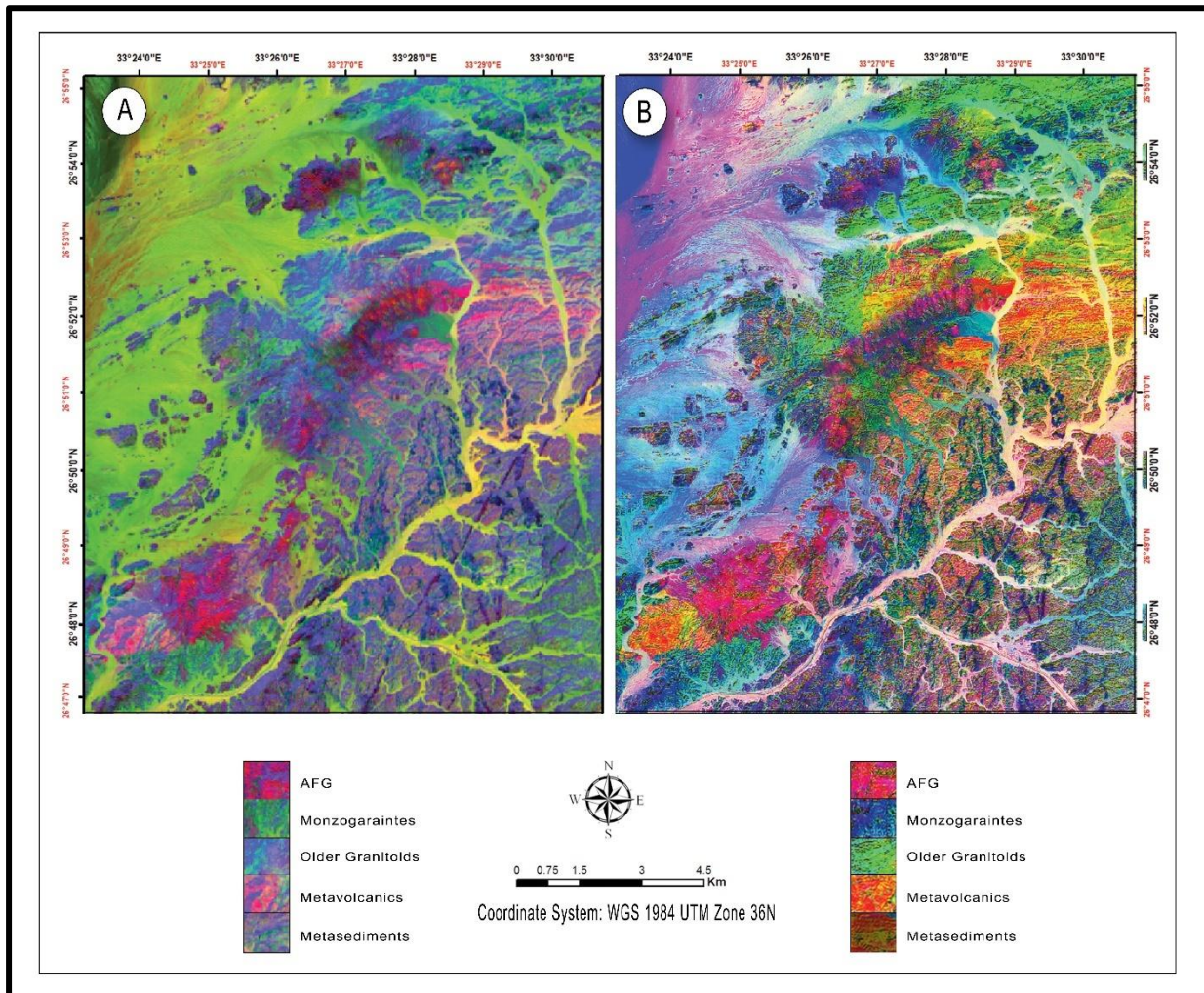
Fig. 4. False color composite images of PC3, PC2, and PC1 in RGB at equalization enhancement stretch using A) Landsat-8 bands, and B) Sentinel-2A bands.

For Landsat-8, the band ratios of b6/b7, b4/b5 and b7/(b7+b4) are stacked together in RGB respectively (Fig. 7a). For Sentinel-2A, the first stacked band ratios are b4/b3, b11/b8a and b11-b12 in RGB (Fig. 7b), while the second stacked group are b11-b4, b11-b12 and (b11+b8a)/b12 in RGB respectively (Fig. 7c).

Due to the mineral affinity of the older granitoids and the difficulty of separating them in the field, a process of separating them using remote sensing techniques from the rest of the rock types is resorted to, and calculations are made to separate them from each other. For Landsat-8, six-band ratios of b6/b7, b7-b6, b6/b3, b7/b6, b6-b5 and ((b3+b5)*b4)/(10*(b7-b6)) are stacked in two RGB images (Fig. 8). While for Sentinel-2A, nine-band ratios are stacked in three RGB images to clarify the differences between the older granitoids rocks, where these successful band mathematical formulas are; (b11*10)/(b12), ((b12+b8a)*b11)/(b12-b8a-b11), b11-b12, b11/(b12-b11), (b8a-b11)*(-10), ((b12-b11)*100)/b3, (b11-b8a)/(b11-b12), b11-b4 and (b11-2)/(b12-2). Nine bands are specifically chosen as the most sensitive Sentinel-2A bands for discriminating the older granitoids in the study area as depicted in Figure (9).
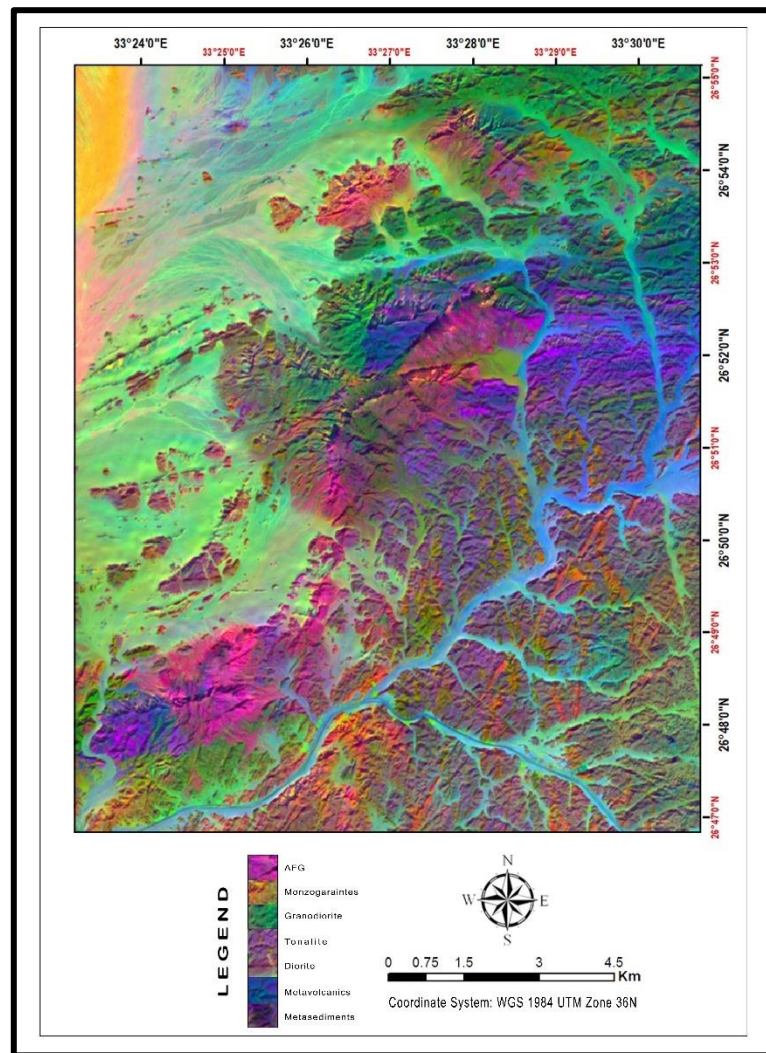
Fig. 5. False color composite image of IC1, IC2, and IC3 in RGB using the Sentinel-2A bands at equalization enhancement stretch.

v. Image Classification

As advanced methods in multivariate statistical classification of satellite images, MLC and SVM are applied to L8 and S2A datasets for lithological classification using ENVI 5.3 software (Fig. 10).

2- Field Observation

The main rock types in Abu Hamr and Abu Kharif area can be classified from the oldest to the youngest as (metasediment, metavolcanic, older granitoids, and younger granites). Metasediments are forming low to moderately elevated hills, which are composed of alternations of greenish to yellowish beds of fine-grained amphibolite and mica schists. These rocks exhibit primary structures as bedding and lineation, and also exhibit secondary structures such as folds, foliations, and joints (Fig. 11a and b).

Metavolcanics are located at the right flank of Abu Hamr, which are manifested as an E-W elongated belt represented by thick sequences of intermediate to basic lava flows. Also, these rocks are present at the left flank of Abu Kharif, which is lower in elevation than that of G. Abu Hamr. The metavolcanics of the investigated area are intruded by the older granitoids and younger granites with sharp and irregular contacts (Fig. 11c), while the type of contact with the metasediments is hard to notice. Along the contact with the younger rocks, the granites include abundant metavolcanic xenoliths of different shapes and sizes (Fig. 11d).
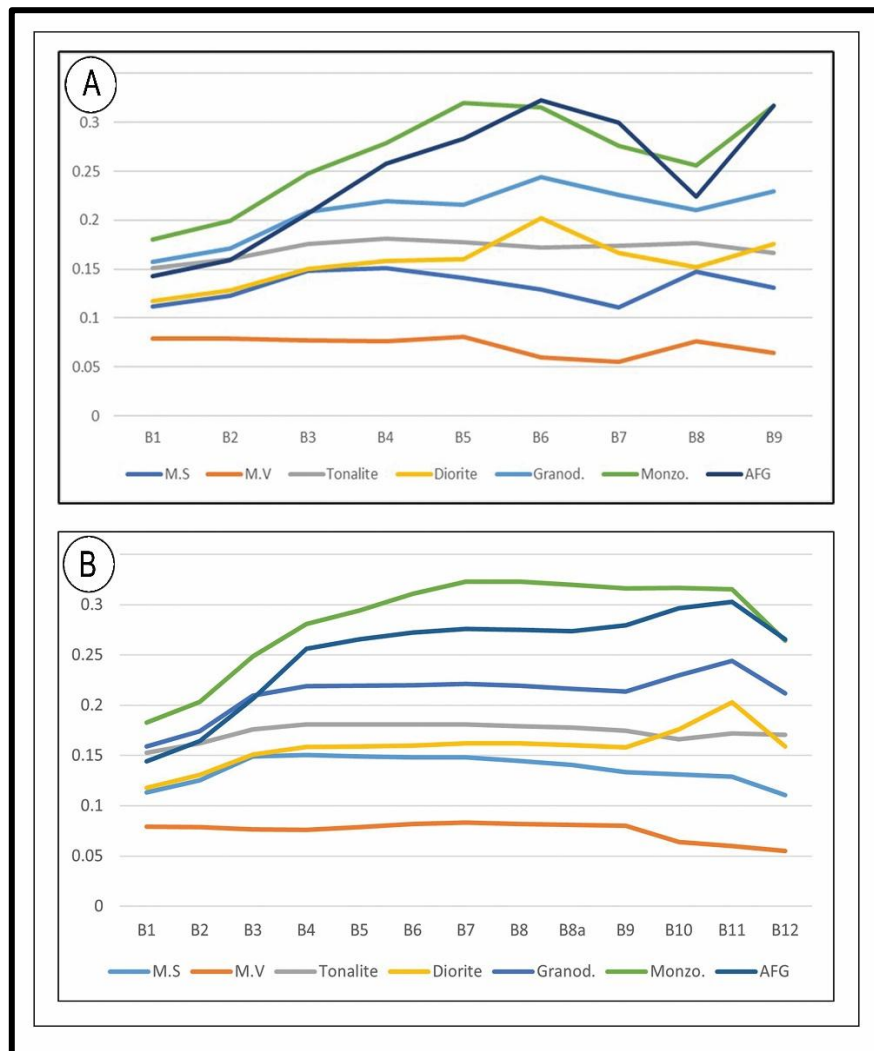
Fig. 6. A) Relative spectral response of rock types with Landsat-8 bands, and B) Relative spectral response of rock types with Sentinel-2A bands, where M.S is metasediments, M.V is metavolcanics, and Granod. It is granodiorite, Monzo. is monzogranites, and AFG is alkali feldspar granites

The older granitoids cover a large part, taking masses of low to medium heights separated by wadies. The older granitoids are dissected by post-granitic acidic and basic dykes and veins with different directions (Fig. 12a). Also, they are weathered, well jointed and showing blocky and bouldery appearance (Fig. 12b). These types of rocks are comprising three varieties including diorite, tonalite and granodiorite.

Younger granites are the highest rock type in the present area, forming the most rugged surfaces and intruding all pre-existing rocks (Fig. 12c). In the mapped area, there are two varieties of younger granites, which are monzogranites and alkali feldspar granites. The alkali feldspar granites have been affected by hydrothermal solutions, especially along fault zones, which are created by the interaction between the rock and natural fluids that permeate the weak fissures of the granites. The alterations in the alkali feldspar granites are mainly hematitization, kaolinitization, chloritization, and epidotization (Fig. 12d).

3- Petrographic Investigation

This section deals with the study of the main microscopic characteristics and relationships of the essential, accessory, and secondary minerals of the rock units in the G. Abu Hamr and G. Abu Kharif area.
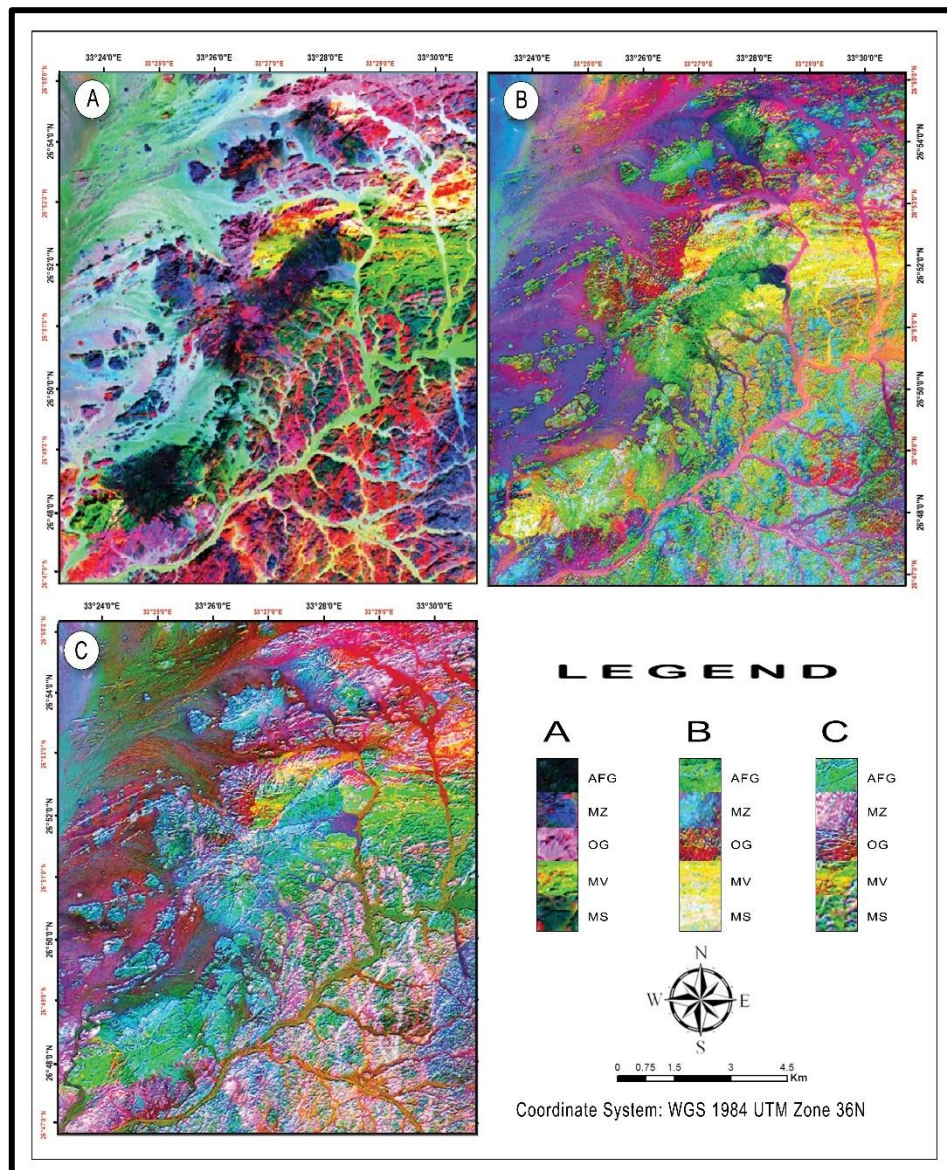
Fig. 7. A) False color composite image of the resulting stacked Landsat-8 band-ratios of b6/b7, b4/b5 and b7/(b7+b4) in RGB respectively at equalization enhancement stretch, B) False color composite image of the resulted from stacked Sentinel-2A band-ratios of b4/b3, b11/b8a and b11-b12 in RGB respectively at equalization enhancement stretch, and C) False color composite image of the resulting stacked Sentinel-2A band-ratios of b11-b4, b11-b12 and (b11+b8a)/b12 in RGB respectively at equalization enhancement stretch.

Starting with the oldest rock units in the area, which are metasediment rocks, they are formed of alternating bands of quartz and amphiboles in the actinolite schists, while these bands are quartz and muscovite in the mica schists exhibiting the schistosity textures (Fig. 13a). Epidote and chlorite are present as accessory minerals in the metasediment rocks.

The metavolcanics range in color from dark green to greenish grey in hand specimens, while under the microscope these rocks range from meta-andesites to meta-basalts, forming thick lava flows of fine to very fine grained, whereas the pyroclastics are less abundant. The mineral assemblages of the metavolcanics indicate regional metamorphism within the range of greenschist facies conditions, which are characterized by the presence of secondary minerals as tremolite-actinolite, chlorite, epidote, zoisite, and saussurite (Fig. 13b).
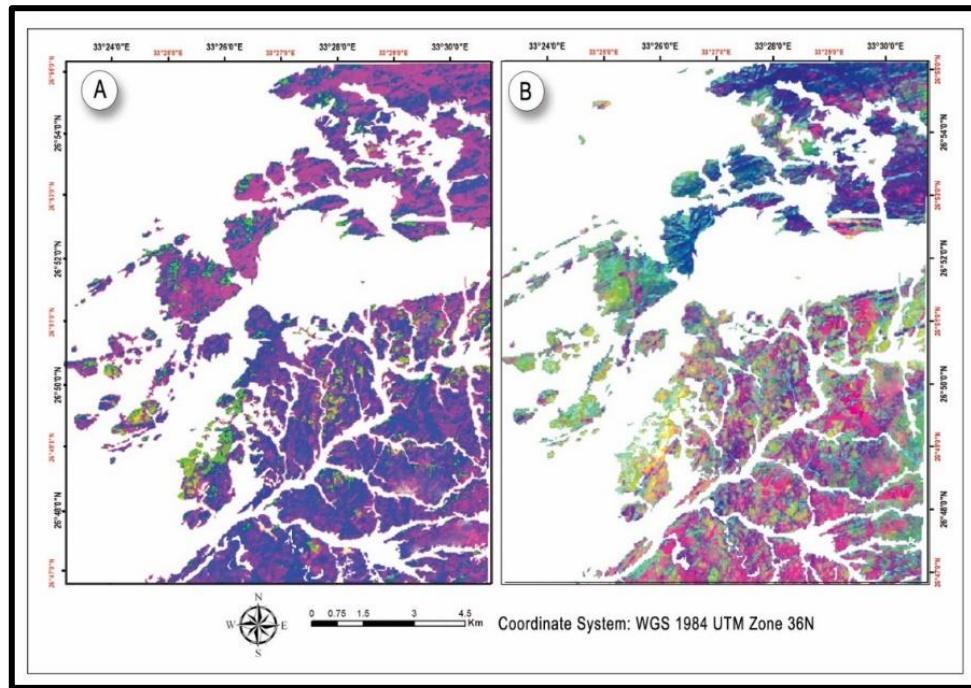
Fig. 8. False color composite images of the resulted stacked Landsat-8 band-ratios: A) b6/b3, b7-b6 and b6/b7 in RGB respectively at equalization enhancement stretch, B) b6-b5, b7/b6 and ((b3+b5)*b4)/(10*(b7-b6)) in RGB respectively at linear 2% enhancement stretch
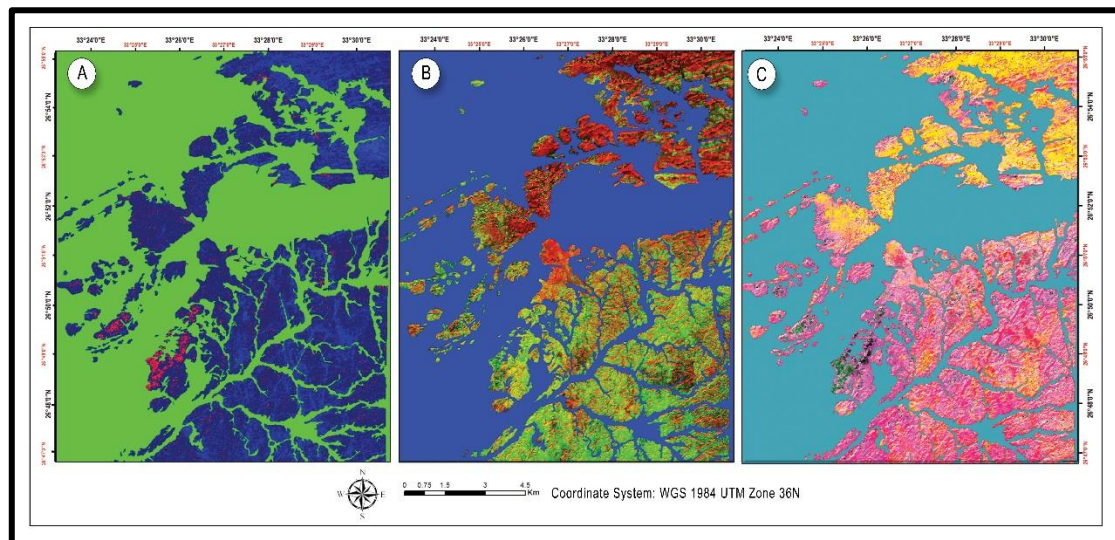

Fig. 9. False color composite images of the resulted stacked Sentinel-2A band-ratios: A) b11-b12, ((b12+b8a)*b11)/(b12-b8a-b11) and (b11*10)/(b12) in RGB respectively at optimized linear enhancement stretch, B) ((b12-b11)*100)/b3, (b8a-b11)*(-10) and b11/(b12-b11) in RGB respectively at equalization enhancement stretch C) (b11-2)/(b12-2), b11-b4 and (b11-b8a)/(b11-b12) in RGB respectively at equalization enhancement stretch.

The studied older granitoids are medium to coarse-grained and characterized by greyish color of diorites and tonalites, and greyish to pinkish granodiorites. Petrographically, all older granitoid varieties display a hypidiomorphic granular texture and essentially consist of plagioclase, hornblende, quartz, K-feldspars, and biotite, but are variable in the ratio of these minerals (Fig. 13c). Saussurite and chlorite are formed due to the alteration of both plagioclase and biotite, respectively (Fig. 13d).
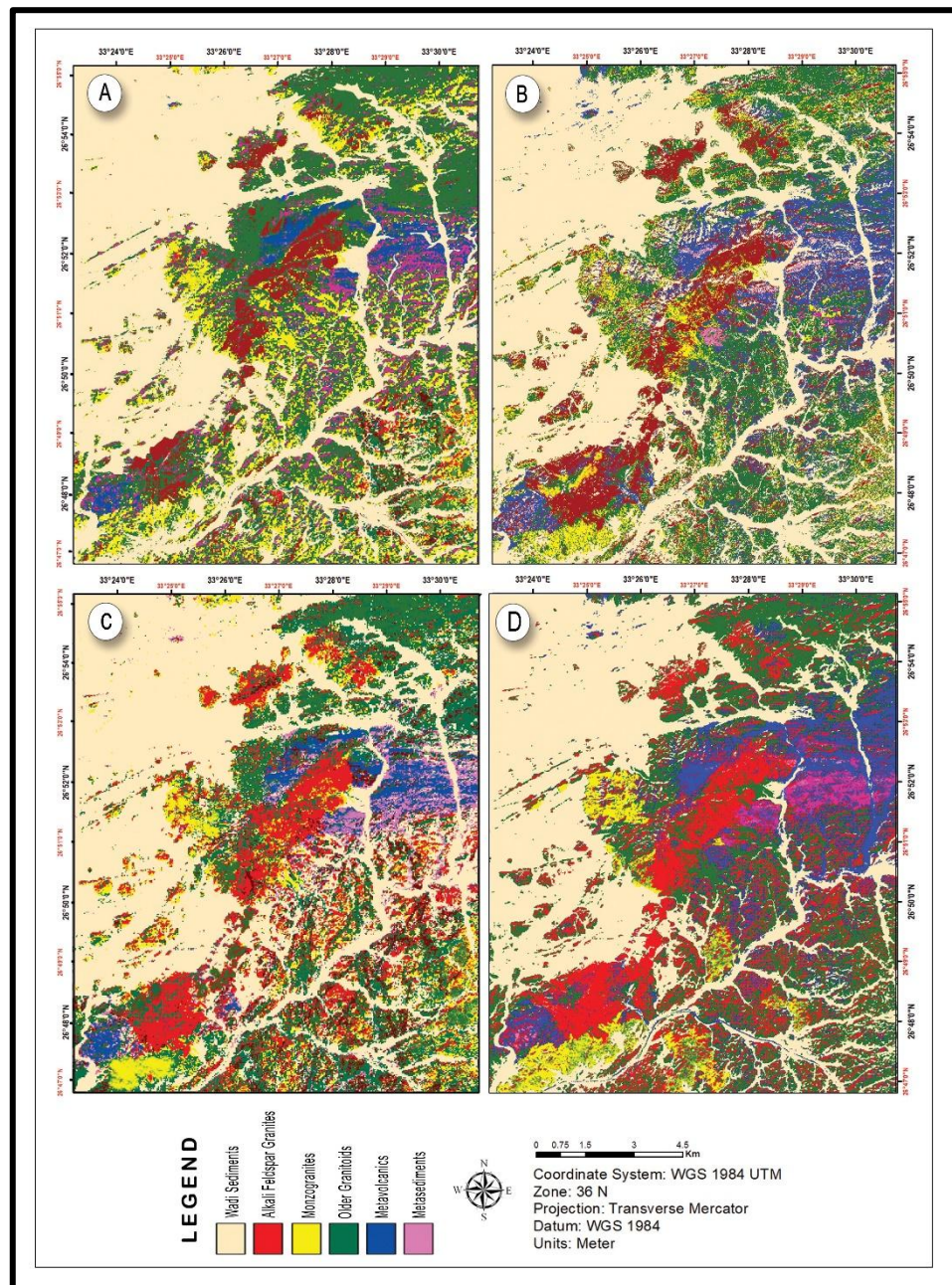
Fig. 10. Lithological classification of different datasets using the MLC method in A) Landsat-8 and B) Sentinel-2A, and the SVM method in C) Landsat-8 and D) Sentinel-2A.

Under the microscope, the younger granites of the study area form some granitic varieties, including monzogranites and alkali feldspar granites, as previously mentioned, where they have equigranular, hypidiomorphic texture and consist of plagioclase (Fig. 14a), K-feldspar, and quartz, in addition to biotite associated with secondary chlorite and opaques. Sphene, zircon, titanite, and opaques are present as accessories (Fig. 14b and c).

Alkali feldspar granites of G. Abu Kharif and most of G. Abu Hamr are geochemically alkaline granites that are considered the youngest phase of granitic magma differentiation present in the area of study (Nossair et al., 2005; Abdel-Hamid et al., 2019). These rocks are similar to the alkali feldspar granites but distinguished by their high abundance of Na-rich minerals and are essentially composed of potash feldspar, quartz, arfvedsonite and aegirine, and a minor amount of plagioclase. Arfvedsonite occurs as subhedral pleochroic from bluish green to blue crystals, which enclose zircon and opaques and are locally altered to riebeckite (Fig. 14d).

Fig. 11. Photographs in G. Abu Hamr and G. Abu Kharif area, North Eastern Desert, Egypt: a) Primary bedding structures in the metasediments; Looking NE. b) Close-up view showing joints and foliations in the metasediments. c) Sharp intrusive contact of Abu Hamr metavolcanics with younger granites; Looking SW. d) Close-up view showing metavolcanic xenolith in older granitoids.
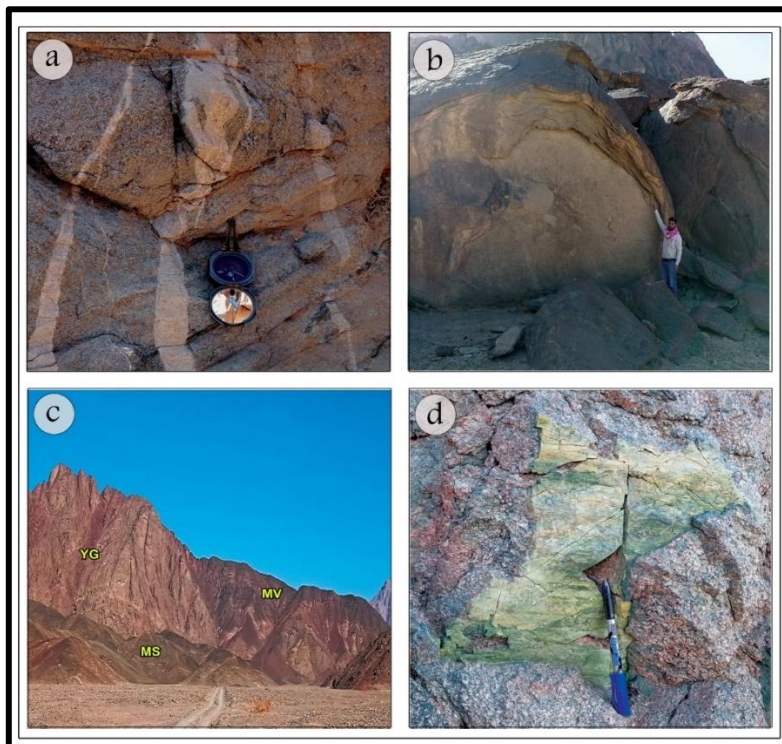

Fig. 12. Photographs in G. Abu Hamr and G. Abu Kharif area, North Eastern Desert, Egypt: a) Close-up view showing aplite veins striking NNE-SSW in older granitoids. b) Exfoliated blocky and bouldery appearance of older granitoids; Looking S. c) Contacts between younger granites (YG), metavolcanics (MV), and metasediments (MS) of G. Abu Hamr; Looking NW. d) Close-up view showing green tint of epidotization in alkali feldspar granites.
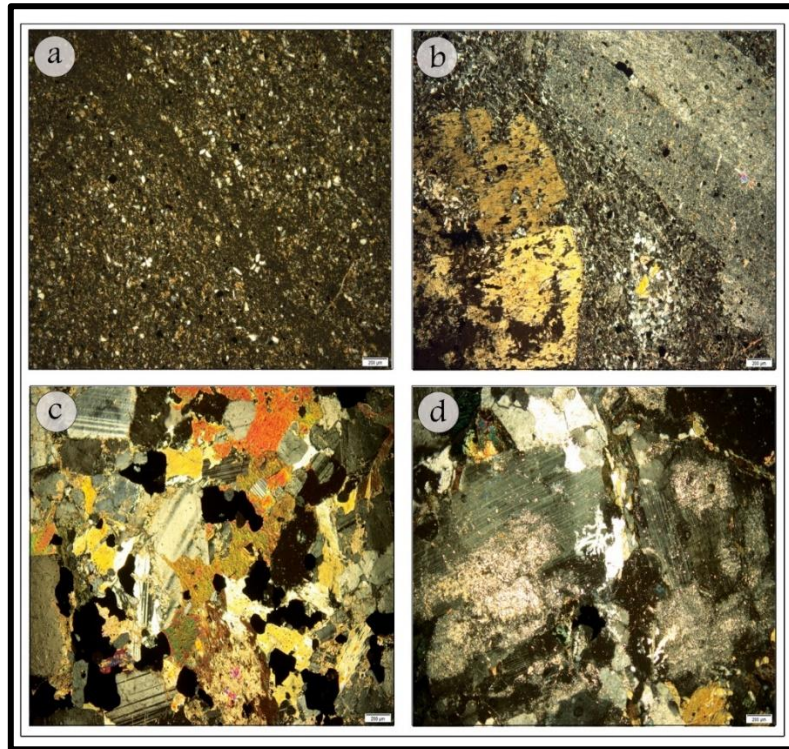
Fig. 13. Photomicrographs in G. Abu Hamr and G. Abu Kharif area, North Eastern Desert, Egypt: a) Muscovite and quartz exhibiting schistose texture in the metasediments, C.N. b) Phenocryst of actinolitic-hornblende in sassuritized plagioclase in groundmass of quartz and plagioclase in metavolcanics, C.N. c) Irregular flake of biotite with partial transformation of hornblende to biotite in older granitoids, C.N. d) Plagioclase showing sassuritization in older granitoids, C.N.
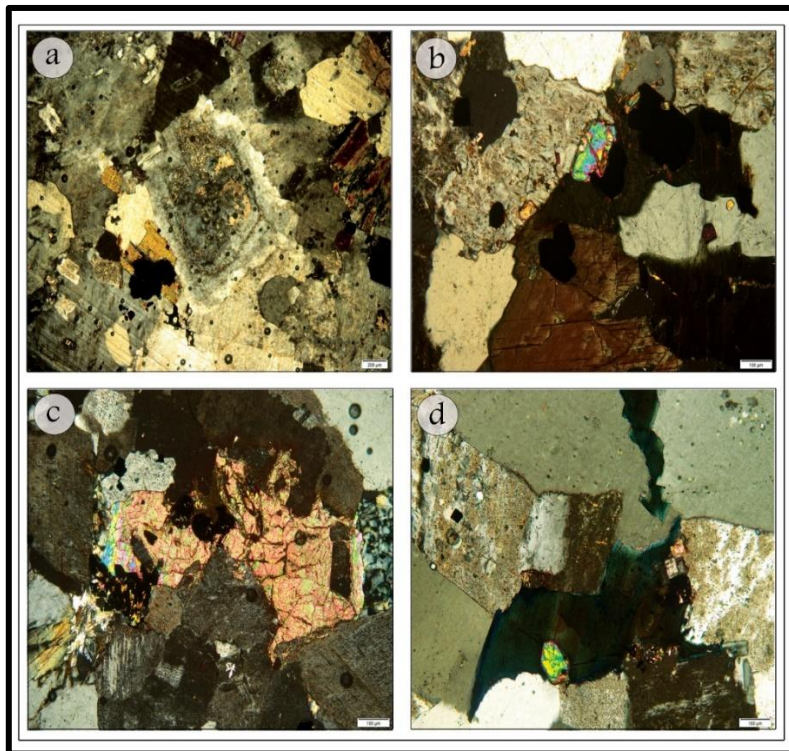

Fig. 14. Photomicrographs in G. Abu Hamr and G. Abu Kharif area, North Eastern Desert, Egypt: a) Zoned plagioclase associated with biotite in monzogranites, C.N.; b) Euhedral crystal of zircon associated with perthite and hornblende in alkali feldspar granites, C.N.; c) Anhedral crystal of titanite associated with perthite and chlorite, C.N.; d) Crystal of zircon included in riebeckite mineral that shows bluish green interference color in alkaline granites, C.N.

According to previous literature, detailed processing of Landsat-8 and Sentinel-2A satellite images, field examination of rock types, and alterations, in addition to further petrographic investigations, will identify rock-associated minerals. The most appropriate geological map of the G. Abu Hamr and G. Abu Kharif area can be expressed in Figure 15.
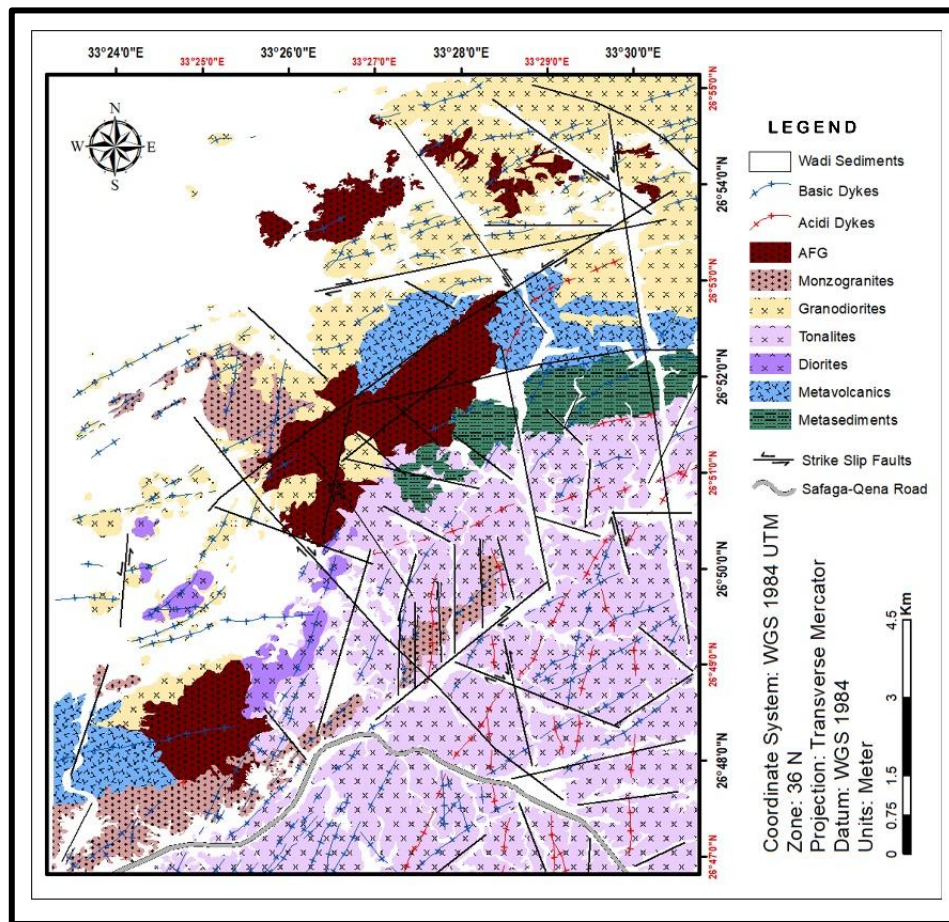

Fig. 15. Geological map of G. Abu Hamr and G. Abu Kharif area, North Eastern Desert, Egypt.

4- Lineaments Extraction

Manual lineaments are identified through visual interpretation of the high-resolution image of the Shuttle Radar Topography Mission (STRM), which is merged with the georeferenced Google Earth map that is divided into eight segments to increase the visibility of its lineaments. Density analysis has been conducted on manually extracted lineaments in the study area, and the results are shown in Figure 16.

For the automated extraction of lineaments, directional filtering is employed to enhance, extract, and classify oriented lineaments in the study area. This method involves a convolution process using a window, typically a (3×3) pixel box, with Sobel-Kernel filters. This technique aims to achieve high accuracy in extracting oriented lineaments, leveraging the directional nature of the Sobel kernel, which provides an effective and efficient means to evaluate lines in main directions (Süzen and Toprak, 1998). Four filtered images corresponding to the main directions N-S, E-W, NE-SW, and NW-SE are generated and used as input images for the auto-extraction methods (Table 5). The automatic lineament extraction approach utilizing the PCI Geomatica LINE algorithm successfully extracts numerous lineaments from Landsat-8 and Sentinel-2A data, as illustrated in Figures 17 and 18.

The manually and automatically extracted lineaments from both Landsat-8 and Sentinel-2A data give similar results for the major lineaments. As shown in Figures 16-18, it has been noticed that the maximum number of lineaments is in the NE-SW and E-W directions in both manual and automatic lineament extraction maps. Unlike the automatic lineaments extraction,

Mohammed A. Soliman *et al…….*

the manual method is more accurate and provides satisfying results, but it takes a lot and a lot of time, unlike the automatic method.

Table 5: Sobel-Kernels in the principal directions used in automatic lineaments extraction.

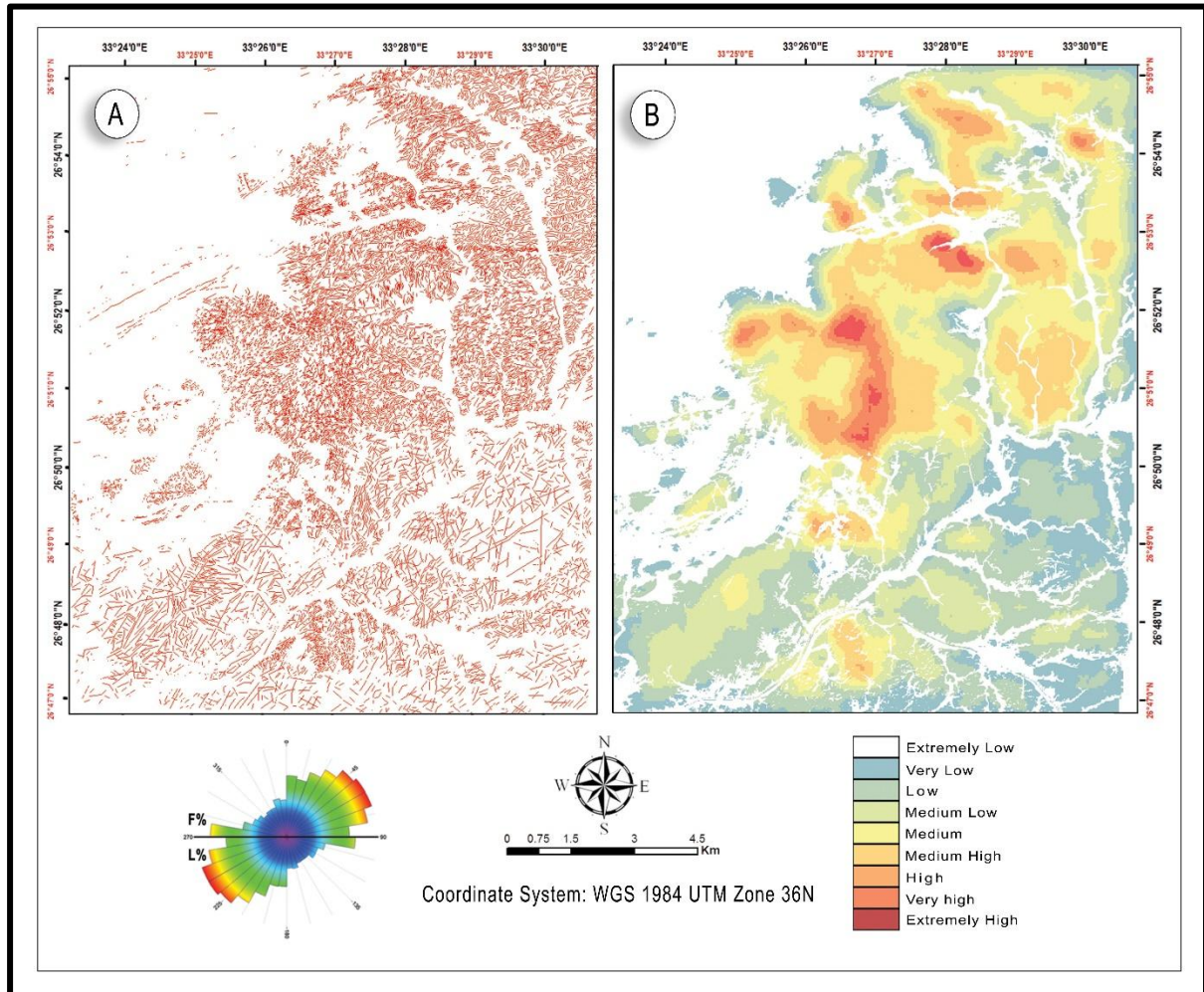| Direction	N-S	NE-SW	E-W	NW-SE
Sobel Kernels	-1 -1 -1	0 1 1	-1 0 1	-1 -1 0
	0 0 0	-1 0 1	-1 0 1	-1 0 1
	1 1 1	-1 -1 0	-1 0 1	0 1 1

Fig. 16. A) Total number (F%) and length (L%) of the manually extracted lineament overlapped over the high-resolution georeferenced Google Earth map of the study area. B) Density map of the manually extracted lineaments of G. Abu Hamr and G. Abu Kharif area, North Eastern Desert, Egypt.

Conclusion

In an attempt to reach the optimal mapping of the G. Abu Hamr and G. Abu Kharif area through unconventional methods that can save a lot of effort and time, multi-processing techniques of Landsat-8 and Sentinel-2A images are used by studying the sensitive and high-response bands. These bands are identified based on the analyzed spectral behavior and the resampled spectral curve. Mathematical formulas are then created, allowing for the separation and distinction of rock types, especially those that have a close similarity in mineral composition. Advanced methods of satellite image analysis are also used based on the multivariate approach, which separates pixels that have the same common values and characteristics. It is found that the best results, through which the final geological and structural lineament maps were reached through the use of remote sensing techniques, in comparable to the field and petrographic studies as follows:
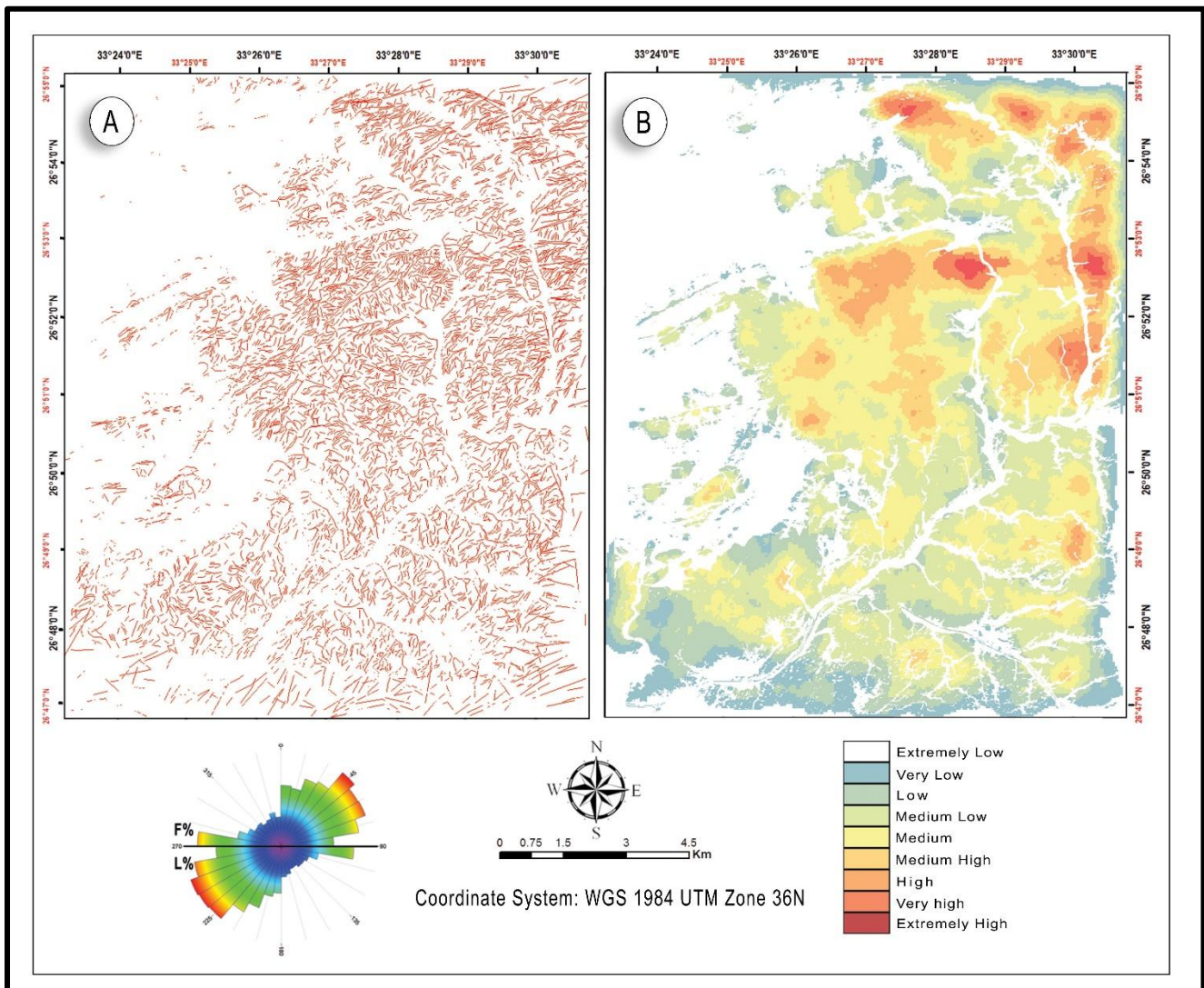
Fig. 17. A) Total number (F%) and length (L%) of the automatically extracted lineament overlapped over the directional filters map of panchromatic band 8 of Landsat-8, B) Density map of the automatically extracted lineaments of Landsat-8.

Studying the images resulting from MNF, PCA, and ICA techniques provides more than 90% of the spectral information in the first three high-order bands. It is possible to separate and distinguish between the younger granites and the rest of the rocks in the area, while the created band ratio formulas are used to distinguish the older granitoid varieties. Using MLC and SVM, similar pixel classification, satisfactory results are obtained regarding the distinction between older rocks represented by the distinction between metasediments and metavolcanics.

The manual extraction method outperforms automatic lineament extraction in terms of accuracy, delivering more satisfactory results. However, in automatic extraction, superior results are achieved due to the enhanced spatial resolution of the satellite image; here it can be said that in the current study, Sentinel-2A images return better results in automated structural lineaments mapping as the 10 meters band of Sentinel-2A highlights the linear structures with better accuracy than those shown by the 15 m panchromatic band of Landsat 8.

As a general, the results of the geological and structural lineament maps obtained show a good correlation with what was studied in the field and under the microscope, as well as the efficiency of remote sensing techniques in identifying the different rock units in G. Abu Hamr and G. Abu Kharif areas.
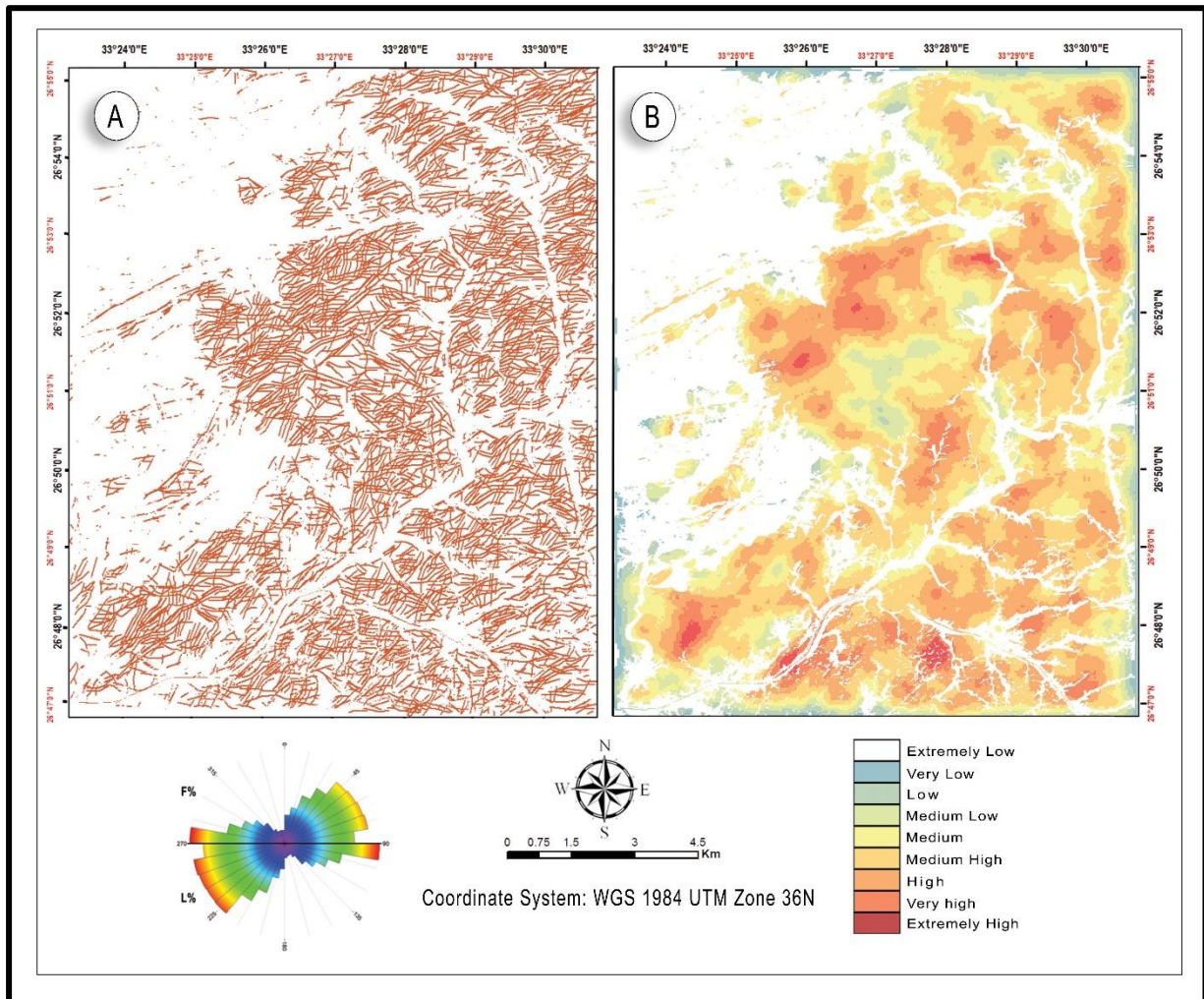
Fig. 18. A) Total number (F%) and length (L%) of the automatically extracted lineament overlapped over the directional filters map of panchromatic band 8 of Sentinel-2A, B) Density map of the automatically extracted lineaments of Sentinel-2A image

References

Abdel-Hamid, H., Abdel Kader, Z., El Manawi, A. and Abdel Warith, A., 2019. Gabal Abu Hamr Pluton: An Example of A-Type Anorogenic Peralkaline Granites in Egypt. Egyptian Journal of Geology, Vol. 63, pp. 291-305.

Abdelmalik, K.W., 2020. Landsat 8: Utilizing Sensitive Response Bands Concept for Image Processing and Mapping of Basalts. The Egyptian Journal of Remote Sensing and Space Science, Vol. 23(3), pp. 263-274. https://doi.org/10.1016/j.ejrs.2019.04.004.

Abdelmalik, K., Abdelghany, O., Fowler, A., Al Azzani, A. and Abu Saima, M., 2023. Applications of Sentinel-2 Remotely Sensed Data to Assist Stratigraphic Subdivision of a Paleogene Carbonate Sequence, UAE, Oman. Seventh International Conference on Engineering Geophysics, Al Ain, UAE. https://doi.org/10.1190/iceg2023-082.1.

Abdelmalik, K.W., and Abd-Allah, A.M.A., 2018. Integration of Remote Sensing Technique and Field Data in Geologic Mapping of an Ophiolitic Suture Zone in Western Arabian Shield. Journal of African Earth Sciences, Vol. 146, pp. 180-190. https://doi.org/10.1016/j.jafrearsci.2017.10.006.

Abdel Wanees, N.G., El-Sayed, M., Khalil, K.I. and Khamis, H.A., 2021. Petrogenesis of Contrasting Magmatic Suites in the Abu Kharif Area, Northern Eastern Desert, Egypt: Implications for Pan-African Crustal Evolution and Tungsten Mineralization. Geological Magazine, Vol. 159, pp. 441-467. https://doi.org/10.1017/S0016756821001047.

Al Amri, S.S., Kalyankar, N.V. and Khamitkar, S.D., 2010. Linear and Non-Linear Contrast Enhancement Image. International Journal of Computer Science and Network Security (IJCSNS), Vol. 10, pp. 139-143.

Bety, A.K.S., 2022. Discrimination Different Lithological Units Using a Remote Sensing Application: A Case Study in the Dokan Area, Kurdistan Region – Iraq, Journal of Water and Land Development, No. 55, pp. 109–114. https://doi.org/10.24425/jwld.2022.142312.

Bety, A.K.S., Al-Jawadi, A. and Ismaeel, O.A., 2022. Lineament Analysis by Using Remote Sensing and GIS Technique of Sangaw Area, Kurdistan Region, NE Iraq, No. 55, pp. 150-161. https://doi.org/10.46717/igj.55.2C.11ms-2022-08-24

Chen, X., Warner, T.A. and Campagna, D.J., 2007. Integrating Visible, Near-Infrared and Short-Wave Infrared Hyperspectral and Multispectral Thermal Imagery for Geological Mapping at Cuprite, Nevada. International Journal of Remote Sensing, Vol. 110, pp. 344-356. https://doi.org/10.1016/j.rse.2007.03.015.

Crowley, J.K., 1986. Visible and Near Infrared Spectra of Carbonate Rocks: Reflectance Variations Related to Petrographic Textures and Impurities. Geophysical Research, Vol. 91, pp. 5001-5012.

Crowley, J.K., Brickey, D.W. and Rowan, L.C., 1989. Airborne Imaging Spectrometer Data of the Ruby Mountains, Montana: Mineral Discrimination Using Relative Absorption Band-Depth Images. Remote Sensing of Environment, Vol. 29, pp. 121-134. https://doi.org/10.1016/0034-4257(89)90021-7.

Drusch, M., Del Bello, U., Carlier, S., Colin, O., Fernandez, V., Gascon, F., Hoersch, B., Isola, C., Laberinti, P., and Martimort, P., 2012. Sentinel-2: ESA's Optical High-Resolution Mission for GMES Operational Services. Remote Sensing of Environment. Vol. 120, pp. 25-36. https://doi.org/10.1016/j.rse.2011.11.026.

El Gaby, S., 1994. Geology and Tectonic Framework of the Pan African Orogenic Belt in Egypt. 2nd International Conference on Geology of the Arab-World, Cairo, Abs., pp. 66-68.

El-Hadidy, Sh.M., Alshehri, F., Sahour, H., and Abdelmalik, K.W., 2022. Detecting Hydrocarbon Micro-Seepage and Related Contamination, Probable Prospect Areas, Deduced from a Comparative Analysis of Multispectral and Hyperspectral Satellite Images. Journal of King Saud University - Science, Vol. 34, No. 6, 102192. https://doi.org/10.1016/j.jksus.2022.102192

El Sundoly, H.I., 2016. Stress Analysis and Radioactivity of Gabal Abu Hamr Younger Granites, Northern Eastern Desert, Egypt. Egyptian Journal of Geology, Vol. 60, pp. 231-250.

Envi Tutorials, 2000. Hands-On Tutorials of the Environment for Visualizing Images (ENVI). Research Systems, Inc., United States, 590 P.

Farag, K.S.I., Howari, F.M., and Abdelmalik, K.W., 2019. Imaging of Hydrothermal Altered Zones in Wadi Al-Bana, in Southern Yemen, Using Remote Sensing Techniques and Very Low Frequency–Electromagnetic Data. Arabian Journal of Geosciences, Vol. 12, No. 18, p. 1-16. https://doi.org/10.1007/s12517-019-4702-8.

Foody, G.M. and Mathur, A., 2004. A Relative Evaluation of Multiclass Image Classification by Support Vector Machines. IEEE Transactions on Geoscience and Remote Sensing, Vol. 42, pp. 1335-1343.

Fowler, A., Baghdady, A., Abdelmalik, K., and Gad, A., 2020. Remote Sensing-Guided Stratigraphic Dissection of an Ediacaran Terrestrial Molasse Basin (Kareim Basin,

Egypt), with Implications for Sedimentary Evolution. Precambrian Research, Vol. 338, 105589. https://doi.org/10.1016/j.precamres.2019.105589.

Gaffey, S.J., 1985. Reflectance Spectroscopy in the Visible and Near-Infrared (0.35-2.55 Microns): application in Carbonate Petrology. Geology, V.13, P.270- 273.

Ge, W., Cheng, Q., Tang, Y., Jing, L. and Gao, C., 2018. Lithological Classification Using Sentinel-2a Data in the Shibanjing Ophiolite Complex in Inner Mongolia, China. International Journal of Remote Sensing, Vol. 10, pp. 683-705.

Ghoneim, S.M., Yehia, M.A., Salem, S.M., and Ali, H.F., 2022. Integrating Remote Sensing Data, GIS Analysis and Field Studies for Mapping Alteration Zones at Wadi Saqia Area, Central Eastern Desert, Egypt. The Egyptian Journal of Remote Sensing and Space Science, Vol. 25, No. 1, pp. 323-336. https://doi.org/10.1016/j.ejrs.2022.02.001.

Gomez, C., Delacourt C., Allemand, P., Ledru, P. and Wackerle, R., 2005. Using ASTER Remote Sensing Data Set for Geological Mapping, in Namibia. Physics and Chemistry of the Earth, Vol. 30, pp. 97-108. https://doi.org/10.1016/j.pce.2004.08.042.

Green, A.A., Berman, M., Switzer, P. and Craig, M.D., 1988. A Transformation for Ordering Multispectral Data in terms of Image Quality With Implications for Noise Removal. IEEE Transactions on Geoscience and Remote Sensing, Vol. 26, No. 1, pp. 65-74.

Gupta, R.P., 2003. Remote Sensing Geology, 3rd Ed. Heidelberg, Springer, Berlin, 655 P.

Jemy, G., Shokry, M.M.F., Farag, K.S.I., Abdelmalik, K.W., 2023. Quadruple Stacked-Based Concept: A Novel Approach for Change Detection. International Journal of Applied Earth Observation and Geoinformation. Vol. 121, July 2023, 103361. https://doi.org/10.1016/j.jag.2023.103361.

Jensen, J.R., 1986. Introduction to Digital Image Processing. Englewood Cliffs, New Jersey, USA.

Kumar, C., Shetty, A., Raval, S., Sharma, R. and Ray, P.K.C., 2015. Lithological Discrimination and Mapping Using ASTER SWIR Data in the Udaipur Area of Rajasthan, India. Procedia Environmental Sciences, Vol. 11, pp. 180-188. https://doi.org/10.1016/j.proeps.2015.06.022.

Maxwell, A.E., Warner, T.A. and Fang, F., 2018. Implementation of Machine-Learning Classification in Remote Sensing: An Applied Review. International Journal of Remote Sensing, Vol. 39, No. 9, pp. 2784-2817.

Mohamed, H.A., Abdel Ghani, M.S., El Mahallawi, M.M. and Shehata, S.A., 2003. Petrogenetic Implications of Mineral Chemistry of Abu Hamr Granitoid Rocks, Northern Eastern Desert, Egypt. 3rd International Conference of Geology of Africa, Assiut University, Vol. 1, pp. 281-300.

Mondal, A., Kundu, S., Chandniha, S., Shukla, R. and Mishra, P., 2012. Comparison of Support Vector Machine and Maximum Likelihood Classification Technique Using Satellite Imagery. International Journal of Remote Sensing, Vol. 1, pp. 116-123.

Nossair, L., Farag, S., Abdel-Warith, A., Omran, A., Bishta, A., Zaher, F., El Wardany, M., Ahmed, A., Hamed, A., Ammar, F., Moharem, A., Mostafa, A., Dessouky, O., and Kourany, E., 2005. Geologic and Radiometric Prospecting for Gabal Abu Kharief Area, North Eastern Desert, Egypt. Scientific, Technologic Documentation and Publishing Council, NMA- IRS-1, 83 P.

O'Leary, D.W., Friedman, J.D. and John, H.A., 1976: Lineament, Linear, Lineation, Some Proposed New Standards for Old Terms. Geological Society of America Bulletin, Vol. 87, pp. 1463-1469. https://doi.org/10.1130/0016-7606(1976)87<1463:LLLSPN>2.0.CO;2

Pour, A. and Hashim, M., 2012. Identifying Areas of High Economic-Potential Copper Mineralization Using ASTER Data in the Urumieh-Dokhtar Volcanic Belt, Iran. Advances in Space Research, Vol. 49, No. 4, pp. 753-769. https://doi.org/10.1016/j.asr.2011.11.028.

Sabins, S. and Lulla, K., 1987. Remote Sensing: Principles and Interpretation. Geocarto International, Vol. 2, 66 P.

Salem, M.M., Yehia, M.A., Omran, A.A., El Sundoly, H.I., Soliman, M. A. and Abdelmalik, K., 2024. Space/Ground-Borne Techniques and Petrographic Microscopic Dissection for Geologic Mapping in Gabal Ras Abda Area, Northeastern Desert, Egypt. Beni-Suef Univ. J. Basic Appl Sci., Vol. 13, No. 44. https://doi.org/10.1186/s43088-024-00502-z

Süzen, M.L. and V. Toprak, 1998. Filtering of Satellite Images in Geological Lineament Analyses: An Application to a Fault Zone in Central Turkey. International Journal of Remote Sensing, Vol. 19, No. 6, pp. 1101-1114. https://doi.org/10.1080/014311698215621

Vincent, R.K., 1997. Fundamentals of Geological and Environmental Remote Sensing: Upper Saddle River, NJ: Prentice-Hall, Inc.

Zhang, X., Pazner, M. and Duke, N., 2007. Lithologic and Mineral Information Extraction for Gold Exploration Using ASTER Data in the South Chocolate Mountains (California). ISPRS Journal of Photogrammetry and Remote Sensing, Vol. 62, pp. 271-282. https://doi.org/10.1016/j.isprsjprs.2007.04.004.